



This is the accepted manuscript made available via CHORUS. The article has been published as:

Electro-optic response in epitaxially stabilized orthorhombic BaTiO_3

BaTiO_3

Marc Reynaud, Pei-Yu Chen, Wenten Li, Therese Paoletta, Sunah Kwon, Dae Hun Lee, Ilya Beskin, Agham B. Posadas, Moon J. Kim, Chad M. Landis, Keji Lai, John G. Ekerdt, and Alexander A. Demkov

Phys. Rev. Materials **5**, 035201 — Published 19 March 2021

DOI: [10.1103/PhysRevMaterials.5.035201](https://doi.org/10.1103/PhysRevMaterials.5.035201)

Electro-optic response in epitaxially stabilized orthorhombic $mm2$ BaTiO₃

Marc Reynaud^a, Pei-Yu Chen^b, Wenten Li^a, Therese Paoletta^a, Sunah Kwon^c, Dae Hun Lee^a, Ilya Beskin^a, Agham B. Posadas^a, Moon J. Kim^c, Chad M. Landis^d, Keji Lai^a, John G. Ekerdt^b and Alexander A. Demkov^{a1}

^aDepartment of Physics, The University of Texas at Austin, Austin, TX 78712

^bDepartment of Chemical Engineering, The University of Texas at Austin, TX 78712

^cDepartment of Materials Science and Engineering, The University of Texas at Dallas, Richardson, TX

^dDepartment of Aerospace Engineering and Engineering Mechanics, The University of Texas at Austin, Austin, TX 78712

Abstract

BaTiO₃ (BTO) is an emergent material in the field of silicon integrated photonics, as its thin films have been demonstrated to have a very large electro-optic (Pockels) coefficient that can be used for optical modulators. However, BTO grown directly on SrTiO₃ (STO)-buffered Si (STO is required for epitaxial growth) initially grows with a polarization direction not suitable for the geometries currently used in photonic devices. Here, we grow BTO on a BaSnO₃ (BSO)-buffered STO substrate to form orthorhombic $mm2$ BTO, which has in-plane polarization orientation needed for photonic devices. Extensive crystalline characterization is done to confirm the high quality of the films, along with electro-optic measurements. Theoretical simulations coupled with the experimental results provide a foundational understanding of the properties of strain-stabilized orthorhombic BTO. Large electro-optic coefficients of 121 pm/V are observed in films as thin as 40 nm.

Introduction

Silicon photonics is a technology combining optical and electronic devices on a single platform. It is rapidly proving itself to be a solution for many fundamental physical constraints that limit the performance of purely electronic circuits. Silicon photonics can be used not only for enabling optical interconnects^{1,2}, but also for new computing paradigms such as neuromorphic, and quantum cryogenic computing^{3,4,5}. The essential element to enable this technology is the optical modulator, a device which modulates the index of refraction of a material with an external voltage. There are several types of optical modulators for silicon photonics, some of which are based on silicon itself, such as plasmon dispersion devices¹. However, many of these devices suffer from having to modulate the absorption of light (the imaginary component of the index) due to the modulation of free carriers, which alters their output intensity^{1,6}. More efficient device architectures require non-standard materials to be integrated onto silicon. A recent example is an electro-optical (EO) modulator based on the Pockels effect in barium titanate (BaTiO₃ or BTO)

¹ demkov@physics.utexas.edu

grown on silicon^{7,8}. The Pockels or linear electro-optic effect is the first order change in the index of refraction under an applied electric field. It has a distinct advantage over other optical modulation methods because it can operate at very low power and very high frequencies^{7,9}, and also does not modulate the absorption of light during operation¹⁰. Bulk BTO has been shown to have one of the strongest known Pockels responses ($r_{42} > 1300 \text{ pm/V}$)¹¹, with high quality thin films showing a response of up to $r_{42} \approx 923 \text{ pm/V}$ ⁷. This is more than an order of magnitude larger than the material that has long been used as the industry standard for electro-optic devices, LiNbO_3 , which has a Pockels coefficient of around 32 pm/V ^{12,13}. LiNbO_3 also suffers from being incompatible with CMOS technology and can only be wafer bonded to silicon using a complicated energy-intensive process^{14,15}. BTO integration on silicon has sufficiently matured that it can readily be deposited on SrTiO_3 (STO)-buffered silicon^{16,17}. However, due to compressive strain in BTO when grown on STO-buffered Si, the crystalline orientation and ferroelectric polarization tend to point out-of-plane (normal to the film surface), gradually transitioning to in-plane only at very large thickness^{16,18,19}. So far, a method of depositing highly epitaxial BTO with all in-plane polarization grown directly on Si (001) has not been demonstrated.

Here, we report the stabilization of highly epitaxial orthorhombic $mm2$ BTO with in-plane polarization using strain engineering. By inserting the appropriate thickness of a strain control layer of BaSnO_3 (BSO) that has a larger lattice constant than BTO, an orthorhombic, single domain, in-plane polarized BTO layer can be formed. Films as thin as 40 nm show a substantial Pockels coefficient of 121 pm/V . This value is approximately four times larger than that of bulk LiNbO_3 , the current industry standard. The work described here uses STO as a substrate. However, recent work by Wang et. al²⁰ showed the direct integration of highly epitaxial BSO on STO-buffered Si, which demonstrates that the results shown here are readily transferable to Si.

In the following sections, we briefly explain the growth and processing of the BTO and BSO layers along with metallic contacts necessary for Pockels measurements. We also show scanning transmission electron microscopy (STEM) results confirming high quality epitaxy and sharp interfaces between the layers; high-resolution reciprocal space maps (RSM) confirming the orthorhombic phase; piezo-force microscopy (PFM) measurements showing that the film has in-plane polarization domains in its as-grown state; and Pockels measurements confirming the in-plane polarization and strong electro-optic effect for a film of only 40 nm thickness. These results are corroborated with phase field modelling and density functional theory (DFT) calculations to give a clearer picture of the EO response in the epitaxially stabilized orthorhombic $mm2$ phase of BTO.

Growth and Characterization of BTO films

First, a double side polished (2SP) STO (001) substrate was degreased with acetone, isopropanol and water. It was then exposed to an ozone environment to remove hydrocarbon residue from the surface. After this, it was loaded into an ultrahigh vacuum transfer line that is attached to a custom DCA 600 molecular beam epitaxy (MBE) growth chamber, a custom built atomic layer deposition (ALD) growth chamber, and an X-ray photoelectron spectroscopy (XPS)

chamber with a VG Scienta R3000 hemispherical analyzer and monochromated Al K α X-rays. The MBE also includes a Staib reflection high energy electron diffraction (RHEED) apparatus with kSA 400 imaging system so that the film can be monitored while being grown. Prior to film deposition, the substrate was annealed in vacuum in the MBE chamber at 600 °C for 30 min as a final cleaning step.

Next, a 7 nm-thick BSO template layer was deposited on the STO substrate by ALD. The ALD BSO growth was performed at 180 °C under 1 Torr, with the growth rate being 0.46 ± 0.03 Å per ALD unit cycle. Barium bis(triisopropylcyclopentadienyl) (heated to 150 °C) and tetrakis(dimethylamino) tin (heated to 40 °C) were used as the precursors for Ba and Sn, respectively; room temperature deionized water was used as the co-reactant. Ultrahigh purity argon was used as carrier and purge gas during the ALD cycles. The ALD-grown BSO template layers were amorphous as-grown and an *in-situ* post-deposition annealing at 650-750 °C in oxygen (1×10^{-5} Torr) was needed to crystallize the films. More details about the ALD BSO growth can be found in our previous work²¹. The 7 nm BSO film is crystallized as a fully relaxed epitaxial layer on STO with a measured in-plane lattice constant of 4.117 Å.

After the ALD-grown BSO was confirmed to be crystalline, 40 nm of BTO was deposited by MBE at 800°C and with an oxygen pressure of 5×10^{-6} torr, using shuttered deposition growth, with both Ba and Ti being evaporated using Knudsen effusion cells in alternating fashion. The film was monitored during growth with RHEED, as shown in Figure 1a. The compositional quality of the film was checked with in situ XPS. Afterward, the crystalline structure of the film was analyzed by X-Ray diffraction (XRD) with a Rigaku Ultima IV X-ray diffractometer. Figure 1b shows an RSM of the (103) diffraction peaks of BTO and STO. It is clear that the BTO is not strained to the STO, as its in-plane reciprocal spacing (Q_x) is not matched to the STO. This is because the BTO is instead strained in-plane to the relaxed BSO layer. Figure 1c shows a rocking curve of the BTO (002) peak showing a full-width at half-maximum of 0.12°, indicating that the film has high crystalline quality. See Supplemental Material Notes 1 and 2 for additional XPS and XRD characterization results. For electro-optic measurements, tungsten contact pads were deposited via DC sputtering with a Cooke Sputtering system after patterning using a photolithographic lift-off process. A schematic layer of the test structure is shown in Figure 1d.

BTO phase analysis

When BTO is grown on a substrate with a larger lattice constant such as BSO, it experiences residual tensile strain. Based on phase field simulations²², one possibility is that this strain will make the film grow in its usual bulk tetragonal phase but with the long c-axis lying in the plane of the film, which results in the so-called *a/c* domain structure. Another possibility is that strain will result in one of the theoretically predicted orthorhombic phases (either *Pmm2* or *Amm2*, depending on the polarization orientation), producing an *a/a* domain structure²³. To determine which crystallographic phase forms in our case, we have performed a high-resolution RSM of the BTO (103/301) reciprocal lattice region shown in Figure 2a. The *mm2* phase of BTO (*a/a* domains) should only have one in-plane lattice constant that is larger than bulk BTO, so only one peak is

expected in the RSM. This is indeed what we observe for our films, with only a single peak in the RSM corresponding to a decreased out-of-plane spacing and an increased in-plane lattice spacing. The $P4mm$ equilibrium bulk phase of BTO, if the long c -axis is laying in-plane, is expected to grow in two domains resulting in two distinct in-plane lattice spacings. The expected splitting in reciprocal space along Q_x is roughly 0.003 \AA^{-1} , with the expected positions of the peaks indicated by black crosses in Figure 2a²⁴. It is clear that such splitting does not occur. This gives strong evidence that our films are in one of the two $mm2$ phases of BTO, and not the $P4mm$ phase, shown in Figures 2b and 2c. For epitaxial $Amm2$ the lattice vectors follow $\vec{a} = \vec{b} \neq \vec{c}$ and $\vec{a} > \vec{c}$ and has $\vec{P} \parallel \langle 110 \rangle$ apart from having a small component along $\pm \vec{c}$, but a reduction in rotation symmetry due to the Ti displacement leads to the $Amm2$ space group. For epitaxial $Pmm2$, the lattice relations are the same as epitaxial $Amm2$, but $\vec{P} \parallel \langle 100 \rangle$ apart from \vec{P} pointing slightly in $\pm \vec{c}$. Note that this is the primitive cell for the epitaxial phase of either the $Amm2$ or $Pmm2$ BTO. It is important to note here that the $mm2$ phases are present because of the epitaxial strain on the BTO film, and not from a low temperature phase transition present in bulk BTO²⁵. A schematic of bulk $Amm2$ BTO is shown in Figure 2d. The lattice constants calculated from the 2D pseudo-Voigt fit of the reciprocal lattice point are (in pseudocubic notation) $a = 4.042 \pm .020 \text{ \AA}$ and $c = 3.990 \pm .006 \text{ \AA}$. This corresponds to an approximately 1.28% tensile strain and are in accordance with the calculations of Li et al.²², which predict that one should have the O_2^F (polarization along $[110]$) $Amm2$ phase of BTO at room temperature. This phase diagram is also discussed in Vaithyanathan et al.¹⁶ See Supplemental Material Note 2 for the details of strain calculations. Another possible source of strain in the BTO is the thermal expansion mismatch during cooling post growth between the BTO and the BSO layers^{20,27}, causing tensile strain in BTO and compressive strain in BSO. However, considering the small thickness of the BSO the effect is likely small, at least when STO is used as a substrate.

In addition to the high-resolution RSM, we have performed cross-sectional high-angle annular dark-field scanning transmission electron microscopy (HAADF-STEM) imaging. This was performed using a JEOL-ARM 200F operated at 200 kV. The convergence semi angle of the electron probe was 25 mrad, and the collection semi angle of the ADF detector was 70-250 mrad. The cross-section STEM specimen was prepared using dual beam focused ion beam FEI Nova 200. With this, we are able to examine the epitaxy between the different layers in the heterostructure. Figure 3a is a large-scale cross-sectional STEM image, while figure 3b is a magnified image. Both are taken along the $[100]$ zone axis of the STO, with figure 3a showing the film is grain free over a large scale while figure 3b shows excellent epitaxy (with misfit dislocations) and sharp interfaces between the different layers. The BTO and BSO layers are in epitaxial registry with the STO substrate. Along with TEM, nano-beam diffraction (NBD) was performed on the sample. This technique is a direct diffraction imaging technique with a small parallel electron beam to limit the beam area, and can be used to extract lattice spacings along with crystal orientation. Figure 3b shows the spot on the film where NBD is performed, and Figure 3c is the resulting diffraction pattern. There is no measurable splitting in the pattern for the BTO

layer, in agreement with the RSM of the (103)/(301) peak indicating that the film is in one of the two $mm2$ phases.

To better understand the phase composition of the BTO thin film, and how the film responds to different external strain as well as electrical boundary conditions, we perform simulations using a phenomenological phase field model to determine the polarization domain structure of our BTO films. This allows us to test what critical strain can stabilize the whole BTO film in the $mm2$ phase. The evolution of the BTO thin film polarization domain morphology is governed by the time-dependent Landau-Khalatnikov equation, coupled with static partial differential equations of the electrical and mechanical equilibrium states^{22,28,29}. The Landau-Khalatnikov equation can be written as $\beta \frac{\partial P_i}{\partial t} = -\frac{\delta F}{\delta P_i}$, where β is the kinetic coefficient, and F is free energy. See Supplemental Material Note 3 for more phase field modelling details. We employ the finite element method^{28,29} to track the evolution of polarization, electric field, electrostatic potential, strain and stress, as a function of time, under isothermal conditions at 298.5 K (room temperature), and with a simulation domain size of $30 \times 30 \times 18$ elements to represent the film. This corresponds to a $30l_0 \times 30l_0 \times 18l_0$ volume, where $l_0 \approx 1 - 2$ nm is the characteristic length (details of how l_0 is determined are in Supplemental Material note 3.1). As shown later, the thickness of our simulation cell is sufficiently large to cover the real experimental sample thickness (40 nm). The in-plane size is also large enough to accommodate the coexistence of different BTO phases as well as domain walls. To simulate the real experimental electrostatic conditions, we use an open circuit boundary condition (O-BC) for the BTO top surface and vary the bottom surface to either have an O-BC or an electrically grounded boundary condition (EG-BC) due to the possible screening by free charges at the BTO/BSO interface induced by interface effects^{30,31} (details in Supplemental Material Note 3). The EG-BC and O-BC at the BTO/BSO interface correspond to two extreme possible interface conductivity states, fully conductive or insulating. As will be shown next, both of these boundary conditions stabilize the $mm2$ phase. To allow for partial strain relaxation in the BTO film, we model tensile strains of 0.5 % and 1.08 % under EG-BC, and strains of 0.38 % and 0.5 % under O-BC. The details of how the strain values are determined and calculation details at different strain values can be found in Supplemental Material Note 3. Following Li et al.²² we use the following notation to represent different BTO domain phases: $\mathbf{P} = [P_1, \delta P, \delta P]$ or $[\delta P, P_2, \delta P]$ in O_1^F ($Pmm2$ phase), $\mathbf{P} = [P_1, P_2, \delta P]$ in O_2^F ($Amm2$ phase), $\mathbf{P} = [P_1, \delta P, P_3]$ or $[\delta P, P_2, P_3]$ in M_1^F (monoclinic phase) and $\mathbf{P} = [P_1, P_2, P_3]$ in M_2^F (monoclinic phase), where δP is a small value. Under 0.500% strain and EG-BC as shown in Figure 4a, we observe a mixed state involving all three domains, where O_1^F regions are present mainly in the upper region, while O_2^F and M_2^F regions are more significant near the bottom surface, where EG-BC allows the P_3 component to survive. The corresponding microscopic lattice structures of orthorhombic O_1^F and O_2^F and monoclinic M_2^F phases are shown, as indicated by the yellow circles. If we increase the strain to 1.080% under EG-BC, as shown in Figure 4b, we observe the disappearance of the M_2^F phase because the out-of-plane polarization (P_3) is completely suppressed. Meanwhile, O_2^F dominates the entire film and only the surface region is in

an intermediate state of O_2^F and O_1^F . The O-BC results, as shown in Figures 4c and 4d, behave similarly as we increase the strain values, resulting in the disappearance of the z polarization component and dominance of the O_2^F phase. However, due to a different boundary condition at the bottom, the M_1^F phase in Figure 3c is found near the center of the film, while the M_2^F phase in Figure 3a is near the bottom. There exists a critical strain in both cases where O_2^F begins to dominate and O_1^F , M_1^F and M_2^F disappear. Comparing Figures 3b and 3d, the critical strain where O_2^F dominates under the EG-BC ($\sim 1.08\%$) is larger than that under the O-BC ($\sim 0.40\%$). What is also important to note here is that regardless of the physical BC of the interface, the BTO will tend towards the $mm2$ phase. To compare with phase field modeling, in-plane piezo-force microscopy (PFM) was performed using a commercial atomic-force microscope (AFM, Park Systems XE-70) and an HF2LI Lock-in amplifier to demodulate the piezo response. The measurement was done with a 1 V AC bias on a virgin film to see if in-plane domains are present in the as-grown films. For in-plane PFM, the polarization must be perpendicular to the cantilever orientation, and oppositely oriented domains will show a 180° contrast in the phase image. The AFM/PFM results are shown in Figure 4e-j, with the relative position between the cantilever and the $[100]$ direction of the film illustrated in Figure 4k (experimental details in Supplemental Material Note 4). From the in-plane phase images (Figures 4f and 4i), we can see that in-plane polarized domains are indeed present in the as-grown state. Comparing figures 4h and 4i shows no direct correspondence between the polarization and topography. The PFM results are in reasonable agreement with the phase field modeling, as they both demonstrate that an as-grown film in tensile strain will exhibit in-plane polarization. Preliminary measurements on the poled film are also shown in Supplemental Material Note 4. It should be noted that real experimental cases may have more complicated electrostatic and mechanical boundary conditions, and this may alter the experimental critical strain when compared with phase field simulations.

The RSM and NBD measurements performed on the BTO thin films confirm that the films are in the $mm2$ phase, whereas the in-plane PFM shows that the film has in-plane polarization in the as-grown state. So far, this phase has only been reported a few times^{32,33,34}. However, in Belhadi et al.³² and Tenne et al.³³, according to the reported lattice constants and error measured, the crystallographic structure of the films described in these reports could also possibly be described as cubic. For Komatsu et al.³⁴, there are grains apparent in their STEM images which can be detrimental for electro-optic applications³⁵. Our films are clearly orthorhombic, with no visible grains on a large scale. Phase field modelling agrees that at this level of tensile strain, the films in this study are in the epitaxially stabilized orthorhombic $mm2$ phase.

Electro-optic properties

Having hypothesized that our BTO films are primarily in the $Amm2$ phase with some residual $Pmm2$ at the surface based on the various characterization results, we now proceed to measure the Pockels coefficient of these films. The linear electro-optic effect is the first order change in the index of refraction with respect to an applied electric field. This is given as

$$n_{ij}(E) = n_{ij}(0) - \frac{1}{2}n_{ij}^3(0)r_{ijk}E_k, \quad (1)$$

where the index k identifies the direction of the applied external electric field and the sum over the repeated index is assumed^{12,36,37}. The Pockels coefficient r_{ijk} indicates the strength of the response in a material and the orientation of the physical parameters that will give a nonzero contribution to the effect^{36,37}. These coefficients are tied to the point group of the crystal. This means that by applying an external electric field, we are able to modify the index ellipsoid of the film, $\sum_{ij}(1/n_{ij}^2)x_ix_j = 1$, either by rotation of the ellipsoid or by distorting it.

The setup used for the Pockels measurement is illustrated in Figure 5a and the important quantities to consider are shown in Figure 5b. They are the pad angle ϕ_E , which determines the direction of the applied electric field, the electric field polarization \vec{E} of the incoming light, the crystallographic direction of polarization \vec{P} (shown here for [110] polarization), and the applied external electric field \vec{E}_A . With the normal incidence transmission geometry in our setup, the ferroelectric polarization of the film must be in-plane in order to interact with the incoming laser beam. The laser used for this experiment is a New Focus TLB 6800 LN diode laser producing 1550 nm wavelength light. The light first passes through a half wave plate to set polarization, and then as it passes through the film it acquires a slightly elliptical component to its polarization, due to the applied electric field. This is then compensated for by the quarter-wave plate to turn back into linearly polarized light with characteristic phase shift $\delta/2$, and finally the light passes through a Glan-Taylor prism used as an analyzer and rotated to gather angle dependent power. This phase shift depends on the film thickness l . The measurement is performed by applying a 35 V DC bias to film via a Keithley B2902A Source/Measure Unit to pole the sample, with a 5 V_{pp} modulating AC voltage (17.3 kHz) applied on top of that via an Ametek Signal Recovery Model 7270 DSP Lock-In Amplifier. The separation between the tungsten pads is 10 μm . With the AC voltage applied, the lock-in amplifier is connected to a Femto OE 200-IN photodetector and used to measure the small phase shift in the thin films induced by the applied electric field. The photodetector is also connected to the Keithley for a measurement of just the input power. See Supplemental Material Note 5 and the literature³⁸ for more details of the electro-optic measurement, including a COMSOL Multiphysics simulation of the applied electric field and electrical testing of the film.

With these considerations taken into account, room temperature measurements were taken for different orientations of incoming light angle θ_i and pad angle ϕ_E . A typical fit of the raw data taken is shown in Figure 5c, along with the equations used in the fit. The plot shows $\Delta P/P$, which can be qualitatively described as the modulated power normalized by the input power. The photodetector takes two different measurements at each value of θ_a . P is measured first, with the photodetector set to DC coupling and the Keithley reads out the intensity. This measurement follows $P = P_0 \sin^2(\theta_a - \theta_0) + B.G.$, where P_0 is the initial laser intensity, θ_a is the angle between the input polarization and the analyzer, θ_0 being any misalignments and the polarization shift due to the DC bias (very small), and B.G. is the background. The shifts are so small for a thin

film that there is no noticeable shift in P when the applied electric field is turned on versus when it isn't on. Also, the AC bias is also modulating the power measured but is undetectable. Next, the photodetector is set to A.C. coupling and ΔP is measured with the lock-in amplifier. This measurement follows $\Delta P = \frac{\partial P}{\partial \theta_a} \delta/2 + \frac{\partial P}{\partial P_0} \tau$, where τ is an error term which can originate from power modulation by effects such as electrical leakage. The phase shift for the AC component $\delta/2$ is the main quantity of interest and is measured using a lock-in technique. Because the Pockels effect is tensorial, it is necessary to rotate either the contact pad angle or the polarization of the incoming light to see if the Pockels response changes as expected. To investigate this, a sweep of the input angle θ_i vs r_{eff} (the effective Pockels coefficient) was performed on a $\phi_E = 45^\circ$ pair of tungsten contacts, and is shown in Figure 5d. The peak positions are at 10° and 100° while a minimum is seen at 55° . The expected peak positions are at 0° and 90° for either $Pmm2$ or $Amm2$ BTO for this geometry, while the minimum is expected at 45° , indicating $\sim 10^\circ$ offset^{12,38}. Considering the polarization axis to be the z -axis of the principal axes of the crystal, $\phi_E = 45^\circ$ and $\theta_i = 10^\circ$ or 100° should give the maximum response from the r_{311} component of $Pmm2$ BTO along with the maximum response from the r_{333}/r_{113} of the $Amm2$ BTO^{12,38,39}. The offset is likely due to a combination of optical, tungsten pad angle, and sample mounting misalignment. The variation of the peak intensity is possibly due to the misalignments or from small scale ferroelectric domain distributions between the pads. Because of this, the two peak values are averaged together. Multiple sets of tungsten pads were measured and an average amplitude of r_{eff} for $\phi_E = 45^\circ$ tungsten pads of 121 pm/V is obtained. See Supplemental Material Note 5 for details of the fitting procedure. The peak intensities and relative intensity ratio from different pairs of tungsten pads for measurements of 10° and 100° input angles showed some variation; the maximum r_{eff} observed is shown in Figure 4d and is approximately 193 pm/V. Multiple measurements at 55° were also done, and r_{eff} values at this input angle were either below 1 pm/V or not extractable. Measurements were also performed with $\phi_E = 0^\circ$ tungsten pads. For $\theta_i = 0^\circ$ with this pad orientation, an average r_{eff} of 30 pm/V was seen, and for $\theta_i = 45^\circ$ an average r_{eff} of 85 pm/V was seen, confirming the expected dependence on θ_i . It is of note that for the $\phi_E = 0^\circ$, $\theta_i = 45^\circ$ geometry we get a moderately large response, in comparison with Abel et. al³⁸. Also, our value is comparable to that of the $\phi_E = 45^\circ$ and $\theta_i = 0^\circ$ response, which is generally the largest response for $P4mm$ BTO. This is a good indication that we have mixed polarization of both $Amm2$ and $Pmm2$ domains and are seeing an enhanced response from the $Amm2$ domain's r_{311} component^{12,36,37}; this result differs slightly from the phase field modelling and RSM presented earlier because it would imply a larger portion of the film is in the $Pmm2$ phase. However, due to a mixed polarization structure in the film, the specific components of the Pockels tensor are difficult to extract. Also, it is possible that the relative strengths of the Pockels tensor components vary more than expected between the different phases of BTO. More work is needed to understand these intricacies. We also note that we can rule out the response seen here as being due to effects that modulate the absorption in the film¹. If absorption was the cause of the modulation in intensity,

the peak of the ΔP would occur at the same point as P peaks, because it would be proportional to the absolute power³⁸. This would make the curve shown in Figure 5c a flat line.

We should emphasize here that we measure a Pockels coefficient that is almost four times larger than that of bulk LiNbO_3 for a 40 nm-thick BTO film. This allows for substantial reductions in both power and size requirements of electro-optic modulators. We also note that for a 40 nm-thick BTO film grown on STO-buffered Si, prior measurements show a negligible Pockels response for the transmission geometry⁴⁰, due to the out-of-plane ferroelectric polarization in thin BTO films grown on Si. In the present case, the BTO film grows immediately with in-plane polarization resulting in a strong Pockels response for the transmission geometry, even at this small film thickness. Our results point to a route for making certain types of electro-optic switches significantly smaller and requiring substantially smaller operating voltages.

To further corroborate our electro-optic measurements, we perform *ab-initio* DFT calculations of the Pockels coefficient for the crystallographic phase that we experimentally observe in our films. See Supplemental Material Note 6 for details of the DFT calculation. We minimize the energy by allowing the strain to determine the c/a ratio. We start with the experimental lateral lattice constant of BSO, $a = 4.116 \text{ \AA}$ ⁴¹, and out-of-plane lattice constant of BTO, $c = 3.99 \text{ \AA}$. We then fully relax the lattice constant c and ionic positions, keeping the lateral dimensions fixed. The BTO unit cell c -axis decreases to 96% of its experimental height, giving a c/a ratio of 0.930. We compare the energies for three polarizations along [100], [110], [111] and find that [110], corresponding to $Amm2$ symmetry, gives the lowest energy. The calculations show a sizable Pockels response for this unit cell.

Both the DFT calculations and electro-optic measurements qualitatively agree with the phase field model. Our DFT calculations reveal that the stable polarization orientation is indeed in the [110] direction at the observed levels of strain, and a sizable Pockels coefficient is predicted. Also, a large Pockels response is indicative of in-plane polarization, and the geometries considered give indication that we have both $Amm2$ and $Pmm2$ phases of BTO present. As stated previously, the electro-optic measurements performed in this geometry works only if the film has in-plane polarization, thus we have strong evidence that the film is in-plane polarized with orthorhombic symmetry, which is corroborated by in-plane PFM measurements.

Conclusions

We have successfully grown the epitaxially stabilized and in-plane polarized unusual $mm2$ orthorhombic phase of BTO on STO by inserting a 7 nm thick strain control BSO layer and confirmed it through a combination of XRD, TEM and Pockels measurements, as well as phase field and density functional theory calculations. The experimental analysis agrees with the theoretical calculations that the film should be in the $mm2$ phase of BTO. The Pockels and in-plane PFM measurements provide strong evidence that the polarization of the film is in-plane. Electro-optic measurements of this orthorhombic BTO show a sizable Pockels coefficient of 121 pm/V for films as thin as 40 nm, four times larger than that of bulk LiNbO_3 . This BTO phase also

has in-plane polarization making it amenable for certain types of electro-optic modulators that require light transmission through the film in hybrid technology using transverse electric (TE) modes in Si or SiN waveguides adjacent to BTO^{7,42,43}. This observed strong Pockels response for very thin films can significantly reduce the size and operating voltage requirements for electro-optic switches that are key elements for optical interconnects and for new computing paradigms such as quantum, neuromorphic, and cryogenic computing^{2,3,4}. Finally, in conjunction with the recent demonstration of BSO on Si²⁰, this work is readily transferable to Si, greatly enhancing its applicability in Si photonics.

Acknowledgements

The work at UT Austin was supported by the Air Force Office of Scientific Research under grant FA9550-18-1-0053. The work at UT Dallas supported in part by Louis Beecherl, Jr. endowment funds. The PFM work was supported by the National Science Foundation (No. DMR-2004536) and Welch Foundation Grant F-1814.

References

1. G.T. Reed, G. Mashanovich, F.Y. Gardes, and D.J. Thomson, *Nat. Photon.* **4**, 518 (2010).
2. M. Heck, H.W. Chen, A.W. Fang, B.R. Koch, D. Liang, H. Park, M.N. Sysak, and J.E. Bowers, *IEEE Journal of Selected Topics in Quantum Electronics* **17**, 333 (2011).
3. K. Vandoorne, P. Mechet, T.V. Vaerenbergh, M. Fiers, G. Morthier, D. Verstraeten, B. Schrauwen, J. Dambre, and P. Beinstman, *Nat. Commun.* **5**, 3541 (2014).
4. F. Eltes, G.E. Villarreal-Garcia, D. Caimi, H. Siegwart, A.A. Gentile, A. Hart, P. Stark, G.D. Marshal, M.G. Thompson, J. Barreto, and J. Fompeyrine, *Nat. Mater.* **19**, 1164 (2020).
5. G.Z. Mashanovich, *Nat. Mater.* **19**, 1135 (2020).
6. R.A. Soref, and B.R. Bennett, *IEEE Journal of Quantum Electronics* **23**, 123 (1987).
7. S. Abel, F. Eltes, J.E. Ortmann, A. Messner, P. Castera, T. Wagner, D. Urbonas, A. Rosa, A.M. Gutierrez, D. Tulli et al., *Nat. Mater.* **18**, 42 (2019).
8. C. Xiong, W.H.P. Pernice, J.H. Ngai, J.W. Reiner, D. Kumah, F.J. Walker, and C.H. Ahn, *Nano Letters* **14**, 1419 (2014).
9. D. Janner, D. Tulli, M. García-Granda, M. Belmonte, and V. Pruneri, *Laser & Photonics Review* **3**, 301 (2009).
10. F. Eltes, D. Caimi, F. Fallegger, M. Sousa, E. O’Conner, M.D. Rossell, B. Offrein, and J. Fompeyrine, *ACS Photonics* **3**, 1698 (2016).
11. M. Zgonik, P. Bernasconi, M. Duelli, R. Schlessler, P. Günter, M.H. Garret, D. Rytz, Y. Zhu, and X. Wu, *Phys. Rev. B* **50**, 5941 (1994).
12. A. Yariv and P. Yeh, *Optical Waves in Crystals* (Wiley Interscience, New York, 1984).
13. R.S. Weis and T.K. Gaylord, *Applied Physics A Solids and Surfaces* **37**, 191 (1985).
14. M. He, M. Xu, Y. Ren, J. Jian, Z. Ruan, Y. Xu, S. Gao, S. Sun, X. Wen, L. Zhou et al., *Nat. Photon.* **13**, 359 (2019).
15. C. Wang, M. Zhang, X. Chen, M. Bertrand, A. Shams-Ansari, S. Chandrasekhar, P. Winzer, and M. Lončar, *Nature* **562**, 101 (2018).
16. V. Vaithyanathan, J. Lettieri, W. Tian, A. Sharan, A. Vasudevarao, Y.L. Li, A. Kochhar, H. Ma, J. Levy, P. Zschack et al., *J. of Appl. Phys.* **100**, 024108 (2006).
17. A.A. Demkov and A.B. Posadas, *Integration of Functional Oxides with Semiconductors*. (Springer, New York, 2014).
18. C. Dubourdieu, J. Bruley, T.M. Arruda, A.B. Posadas, J. Jordan-Sweet, M.M. Frank, E. Cartier, D.J. Frank, S.V. Kalinin, A.A. Demkov, and V. Narayanan, *Nat. Nanotech.* **8**, 748 (2013).
19. M.-H. M. Hsu, D.V. Thourhout, M. Pantouvaki, J. Meersschaut, T. Conard, O. Richard, H. Bender, P. Favia, M. Vila, R. Cid et al., *Applied Physics Express* **10**, 065501 (2017).
20. Z. Wang, H. Paik, Z. Chen, D.A. Muller and D.G. Schlom, *APL Materials* **7**, 022520 (2019).
21. P.-Y. Chen, C.H. Lam, B. Edmondson, A.B. Posadas, A.A. Demkov, and J.G. Ekerdt, *Journal of Vacuum Science & Technology A* **37**, 050902 (2019).

22. Y.L. Li, and L. Q. Chen, *Appl. Phys. Lett.* **88**, 072905 (2006).
23. N.A. Pertsev, A.G. Zembilgotov, and A.K. Tagantsev., *Phys. Rev. Lett.* **80**, 1988 (1998).
24. G.H. Kwei, A.C. Lawson, S.J.L. Billinge, and S.W. Cheong, *The Journal of Physical Chemistry* **97**, 2368–2377 (1993).
25. G. Shirane, H. Danner, and R. Pepinsky, *Phys. Rev.* **105**, 856–860 (1957).
26. M. Acosta, N. Novak, V. Rojas, S. Patel, R. Vaish, J. Koruza, G.A. Rossetti Jr. and J. Rödel, *Applied Physics Reviews* **4**, 041305 (2017).
27. J.A. Bland, *Can. J. Phys.* **37**, 417 (1959).
28. A.Y. Woldman, and C.M. Landis, *International Journal of Solids and Structures* **178-179**, 19 (2019).
29. A.Y. Woldman, PhD Thesis., University of Texas, Austin, 2017.
30. K.D. Frederickson, and A.A. Demkov, *Phys. Rev. B.* **91**, 115126 (2015).
31. A. Ohtomo, and H.Y. Hwang, *Nature* **427**, 423 (2004).
32. J. Belhadi, M. El Marssi, Y. Gagou, Y.I. Yuzyuk, Y. El Mendili, I.P. Raevski, and H. Bouyanfif, *J. of Appl. Phys.* **116**, 034108 (2014).
33. D.A. Tenne, X.X. Xi, Y.L. Li, L.Q. Chen, A. Soukiassian, M.H. Zhu, A.R. James, J. Lettieri, D.G. Schlom, W. Tian, and X.Q. Pan, *Physical Review B* **69**, 174101 (2004).
34. K. Komatsu, I. Suzuki, T. Aoki, Y. Hamasaki, S. Yasui, M. Itoh, and T. Taniyama, *Appl. Phys. Lett.* **117**, 072902 (2020).
35. K.J. Kormondy, Y. Popoff, M. Sousa, F. Eltes, D. Caimi, M.D. Rossell, M Fiebig, P. Hoffmann, C. Marchiori, M. Reinke et al., *Nanotechnology* **28**, 075706 (2017)
36. R.W. Boyd, *Nonlinear Optics* (Academic Press, 2008).
37. B.E.A. Saleh and M.C. Teich, *M.C. Fundamentals of Photonics* (John Wiley & Sons, 1991).
38. S. Abel, T. Stöferle, C. Marchiori, C. Rossel, M.D. Rossell, R. Erni, D. Caimi, M. Sousa, A. Chelnokov, B.J. Offrein, and J. Fompeyrine, *Nat. Commun.* **4**, 1 (2013).
39. S.A. Denev, T.T.A. Lummen, E. Barnes, A. Kumar, and V. Gopalan, *Journal of the American Ceramic Society* **94**, 2699 (2011).
40. K.J. Kormondy, S. Abel, F. Fallegger, Y. Popoff, P. Ponath, A.B. Posadas, M. Sousa, D. Caimi, H. Siegwart, E. Uccelli et al., *Microelectronic Engineering* **147**, 215 (2015).
41. F.G. Kinyanjui, S.T. Norberg, C.S. Knee, I. Ahmed, S. Hull, L. Buannic, I. Hung, Z. Gan, F. Blanc, C.P. Greg, and S.G. Eriksson, *Journal of Materials Chemistry A* **4**, 5088–5101 (2016).
42. J.E. Ortmann, F. Eltes, D. Caimi, N. Meier, A.A. Demkov, Lukas Czornomaz, J. Fompeyrine, and Stefan Abel, *ACS Photonics* **6**, 2677 (2019).
43. P. Castera, D. Tulli, A.M. Gutierrez, and P. Sanchis, *Optics Express* **12**, 15332 (2015).

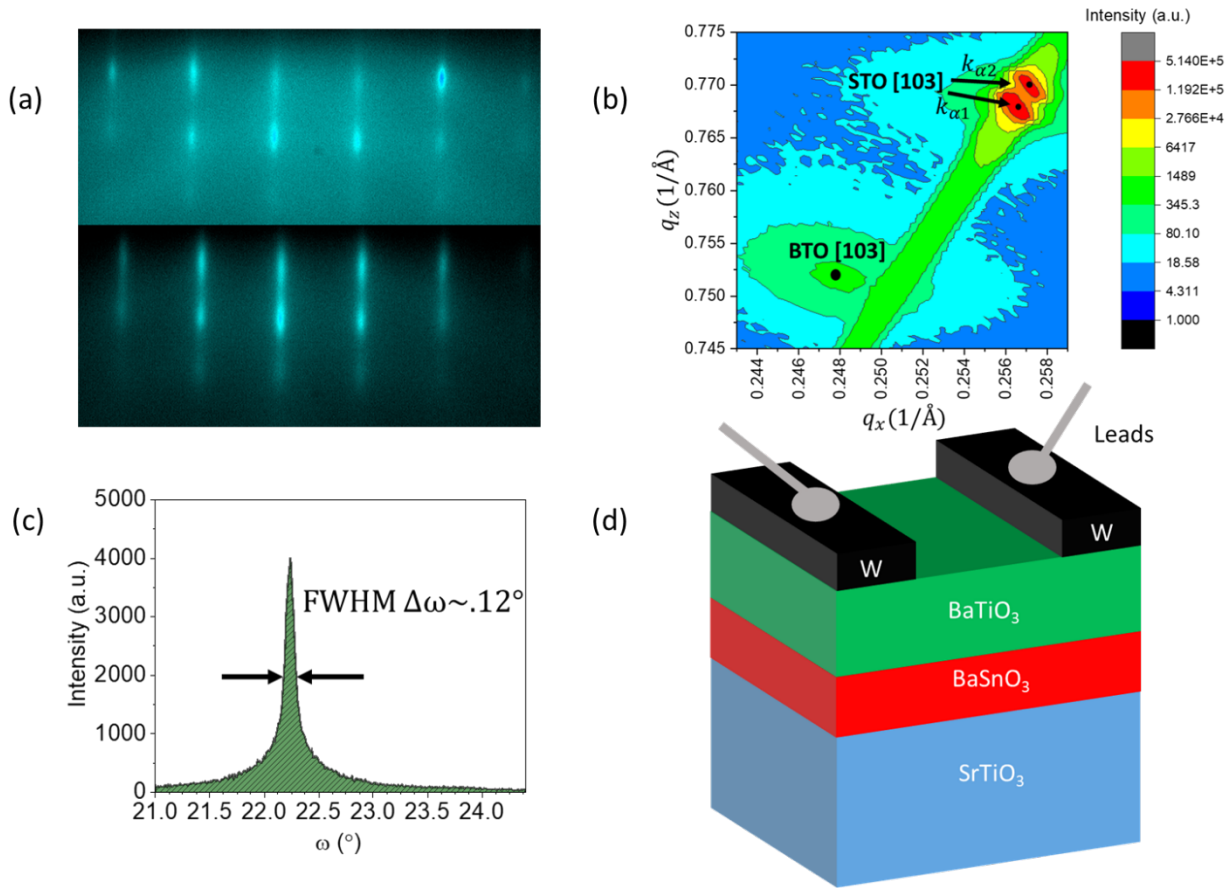


Figure 1: Growth and characterization of the thin film stack. (a) RHEED of 40 nm BTO (above) and 7 nm BSO (below) along the [110] direction of the substrate. (b) RSM of the (103) peak of the STO substrate and BTO film. (c) Rocking curve of the BTO (002) film peak. (d) Final film stack after tungsten deposition also showing electrical leads for applying an electric field. This contact pad orientation allows for in-plane poling of the film during EO measurements.

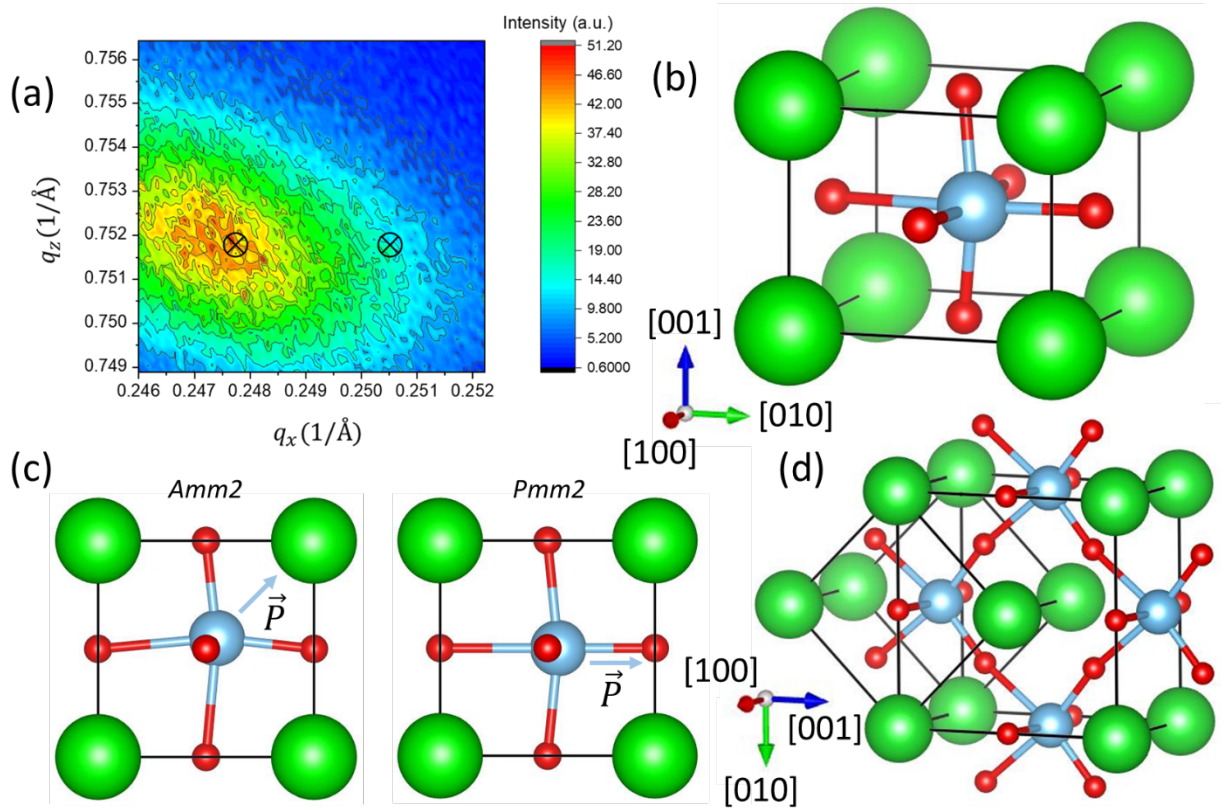


Figure 2: Fine RSM of film and crystalline description. (a) High-resolution RSM of the BTO (103) peak. (b) Crystal structure of epitaxial $Amm2$ phase. For reference, $\vec{a} \parallel [100]$, $\vec{b} \parallel [010]$, and $\vec{c} \parallel [001]$. Green atoms are Ba, blue are Ti and red are O. (c) View along c-axis of both $Amm2$ and $Pmm2$ showing Ti displacement for each phase. (d) Schematic of bulk low-temperature $Amm2$, showing the orthorhombic crystal and the original primitive lattice cell for this phase which is monoclinic²⁶. The lattice vectors follow the standard $\vec{a} \neq \vec{b} \neq \vec{c}$ for an orthorhombic crystal.

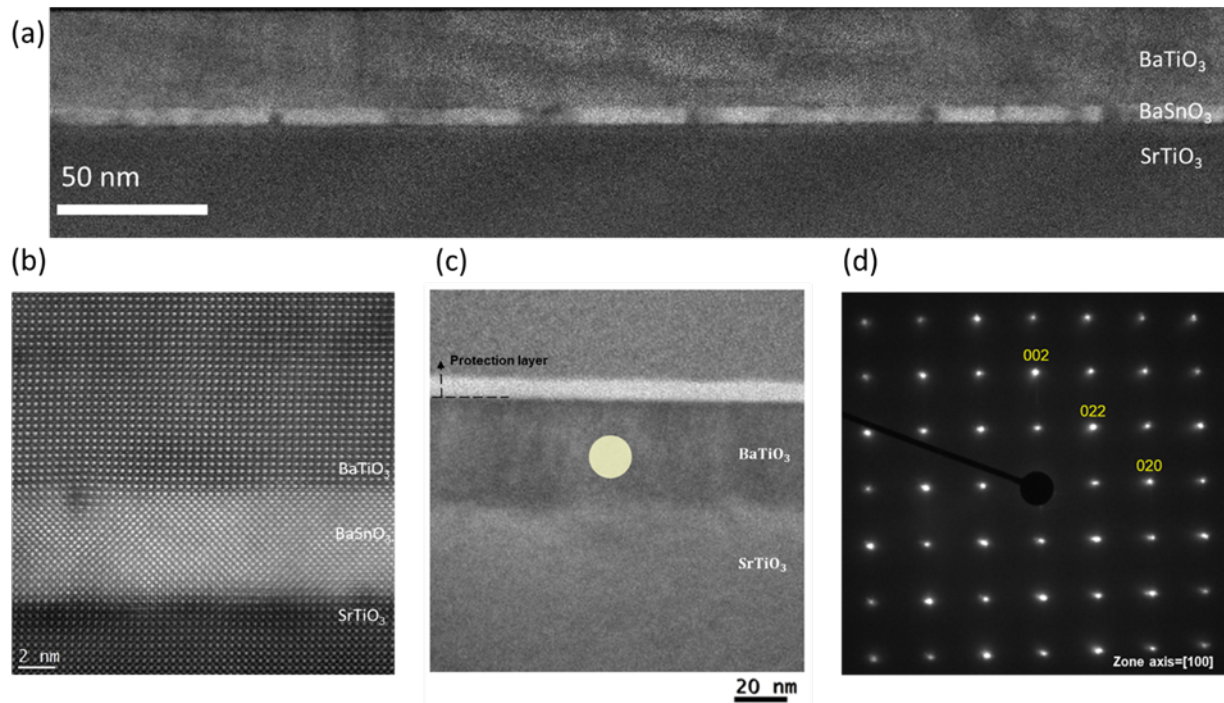


Figure 3: STEM images of the BTO/BSO/STO film stack. (a) Wide view STEM image showing high crystalline quality of BTO across a large region of the film. (b) STEM image of the interface region of the stack along the [100] direction. (c) STEM of stack in the [100] direction showing where nano-beam diffraction is performed indicated by the beige circle. (d) Nano-beam diffraction of the BTO layer.

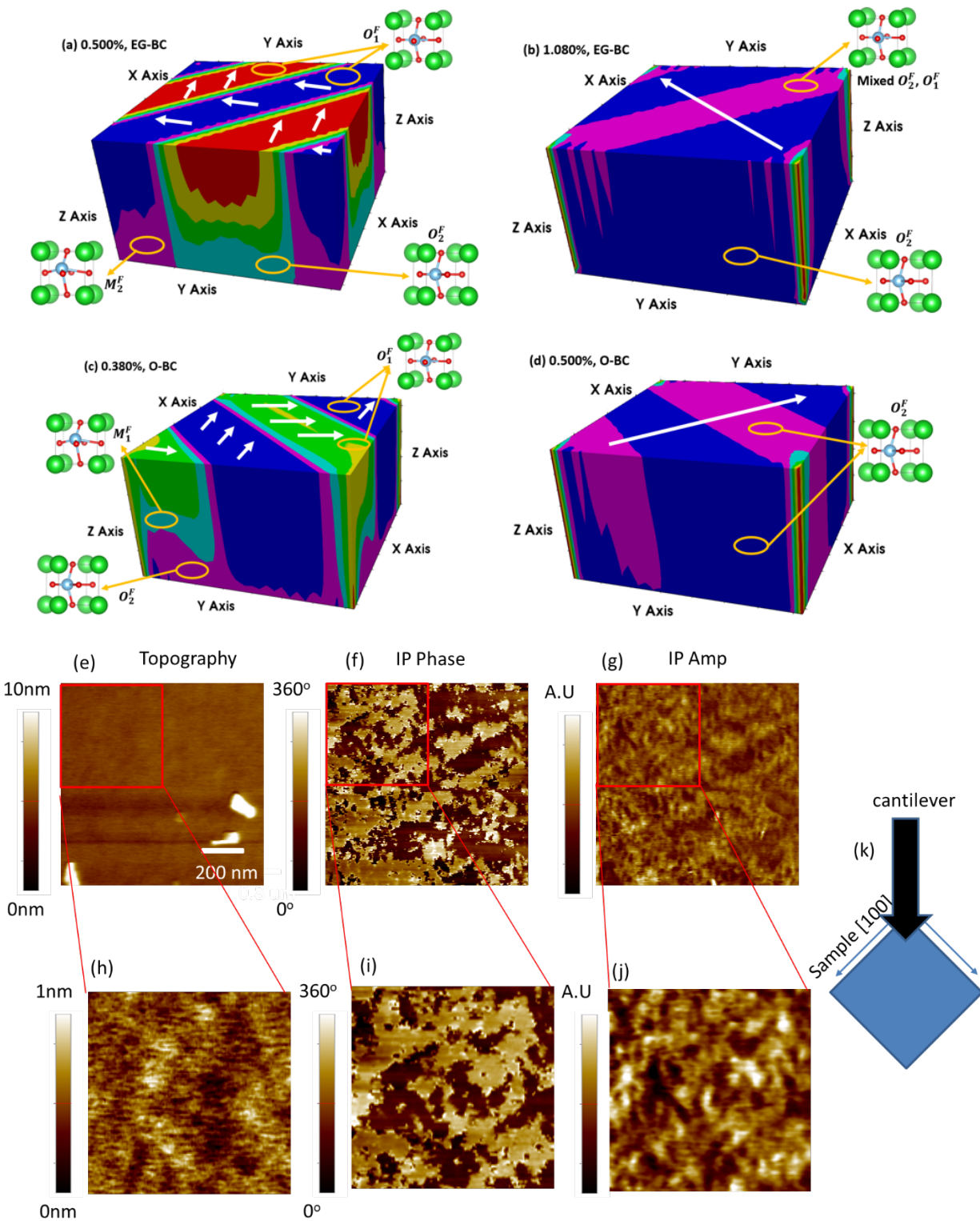


Figure 4: Schematic representations of BTO domain morphology under biaxial tensile in-plane (xy) strain with EG-BC or O-BC (see Supplemental Material note 3 for calculation details). White arrows are the surface polarization vector in each domain. Different color areas represent different domains as well as transition areas. (a) Domain morphology at 0.500% strain under EG-BC in the BTO. 90-degree domain walls are observed on the surface. (b) Domain morphology at 1.080% strain under EG-BC in the BTO. (c) Domain morphology at 0.380% strain under O-BC in the

BTO. 90-degree domain walls are also observed on the surface. (d) Domain morphology at 0.500% strain under O-BC in the BTO. Purple and blue areas both represent O_2^F , but are slightly different in actual values of x and y component. (e-g) Topography, in-plane phase, and amplitude images of the virgin BTO/BSO/STO film. (h-j) Close-up views for (e-g). (k) Illustration of the cantilever orientation with respect to the crystalline axes of the sample in this measurement.

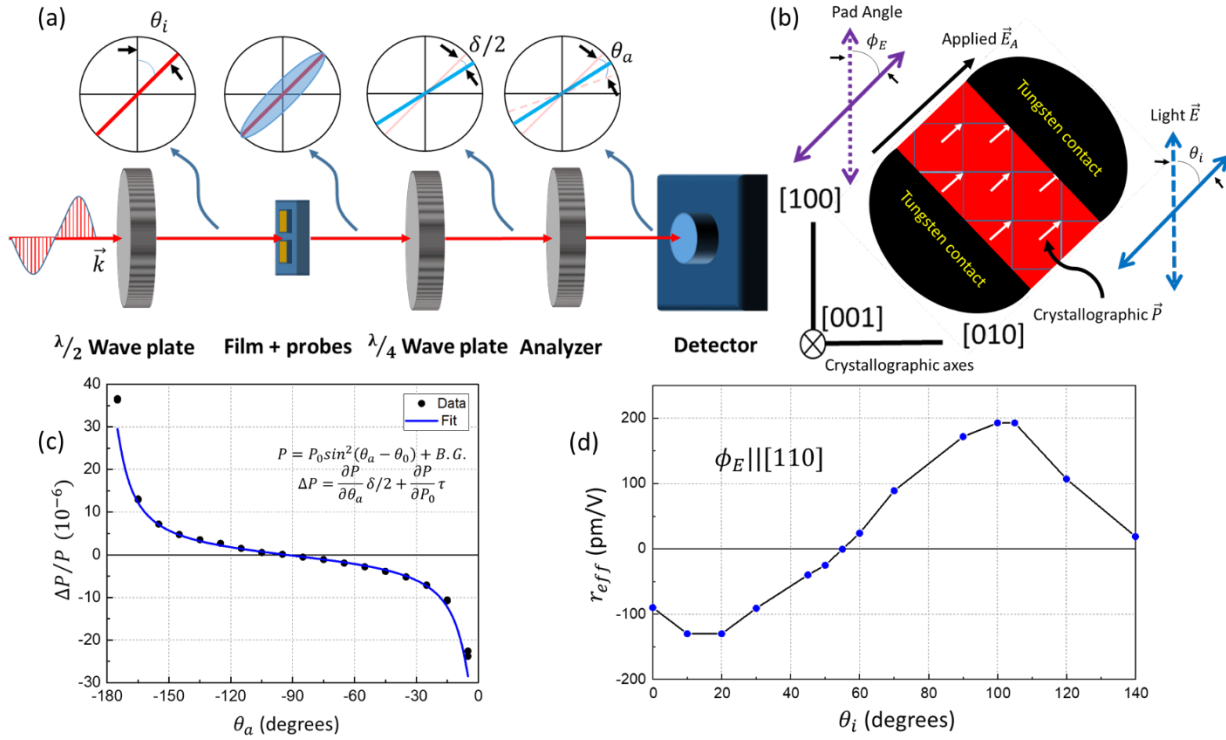


Figure 5: Electro-optic characterization of the film. (a) Schematic of setup used to take Pockels measurements. The insets above the measurement setup components give an illustrative image of what happens to the light polarization as it passes through each component. (b) Schematic showing important quantities of the film during electro-optic measurement. (c) Example fit of the data $\Delta P/P$ collected using this setup from a 45° pad with the incoming light polarization at 100° with respect to the $[100]$ crystallographic axis. (d) Sweep of the Pockels coefficient as a function of the input angle. Peaks are seen at 10° and 100° while at 55° almost no Pockels response was seen, indicating a clear angular dependence on the input polarization.